Comparison of Induction and PM Synchronous Motor Drives for EV Application Including Design Examples

Gianmario Pellegrino, *Member, IEEE*, Alfredo Vagati, *Fellow, IEEE*,
Barbara Boazzo, and Paolo Guglielmi, *Member, IEEE*

Abstract—Three different motor drives for electric traction are compared, in terms of output power and efficiency at the same stack dimensions and inverter size. Induction motor (IM), surface-mounted permanent-magnet (PM) (SPM), and interior PM (IPM) synchronous motor drives are investigated, with reference to a common vehicle specification. The IM is penalized by the cage loss, but it is less expensive and inherently safe in case of inverter unwilled turnoff due to natural de-excitation. The SPM motor has a simple construction and shorter end connections, but it is penalized by eddy-current loss at high speed, has a very limited transient overload power, and has a high uncontrolled generator voltage. The IPM motor shows the better performance compromise, but it might be more complicated to be manufactured. Analytical relationships are first introduced and then validated on three example designs and finite element calculated, accounting for core saturation, harmonic losses, the effects of skewing, and operating temperature. The merits and limitations of the three solutions are quantified comprehensively and summarized by the calculation of the energy consumption over the standard New European Driving Cycle.

Index Terms—Electric machine design comparison, induction motor (IM) drives, permanent-magnet (PM) machines, synchronous motor drives, traction motor drives, variable-speed drives.

I. INTRODUCTION

STATE-OF-THE-ART drive trains for electric vehicles (EVs) are often equipped with induction motors (IMs) or permanent-magnet (PM) synchronous motors [1], [2]. IM drives are adopted for their ruggedness and universal availability. Also, on the control side, field-oriented vector control of IMs is considered a standard, industrially. Moreover, IMs are naturally de-excited in case of inverter fault, and this is very welcome among car manufacturers, for safety reasons.

PM motor drives are considered to have a higher torque density and efficiency, with respect to IMs. Among PM motors, both surface-mounted PM (SPM) and interior PM (IPM) types are adopted for traction [3]. SPM motors for traction have concentrated stator coils [4], i.e., very short end connections

and an easier stator construction. They suffer from eddy-current loss in the PMs at high speed and need structural sleeves for PM retention. Arc magnets such as the ones in Fig. 1(c) can be a problem industrialwise, but different rotor solutions are possible, also contributing to mitigate PM loss [18]. IPM motors require rotors with multiple flux barriers for having a high saliency, such as the one in Fig. 1(b), which might look complicated industrialwise. However, the high saliency is synonymous of a much larger overload torque over the entire speed range [5], a safer back electromotive force in uncontrolled generator operation [6], and little sensitivity to PM temperature.

Synchronous PM drives of both types require a custom control algorithm when flux-weakening operation is required over a wide speed range, as it is the case of traction. The motor magnetic model must be consistently identified for accurate control with the experimental identification tests that are considered cumbersome if compared to the standard ones that are usual for IMs. The recent issue of the rare-earth magnet price volatility is seriously questioning the adoption of PM motor drives [7]. In this scenario, multilayer IPM motors are more suitable for replacing the rare-earth magnets with cheaper ferrite magnets, at least in some cases [9], while SPM and single-layer IPMs are not.

The comparison between IM, SPM, and IPM motor drives for EVs is proposed, at a given vehicle specification and with the three motors having the same outer dimensions of the active parts (stack diameter and length) and the same inverter size (maximum voltage and current). This paper extends the comparison in [5] to include the asynchronous motor, giving further insights on aspects such as skewing and PM temperature.

Three example motors are designed and finite element analysis (FEA) characterized. Their laminations are represented in Fig. 1. Unfortunately, it was not possible to build and test three prototypes to be experimentally compared. However, finite-element simulation can still be considered a consistent instrument of virtual prototyping of electrical machines, accepted industrialwise, as documented in the literature [12], [20], [21], and also for loss evaluation [22].

II. TERMS OF THE COMPARISON

A. Vehicle Specification

As summarized in Fig. 2, EVs require a constant-torque operating region at low speed for starting and uphill march and,
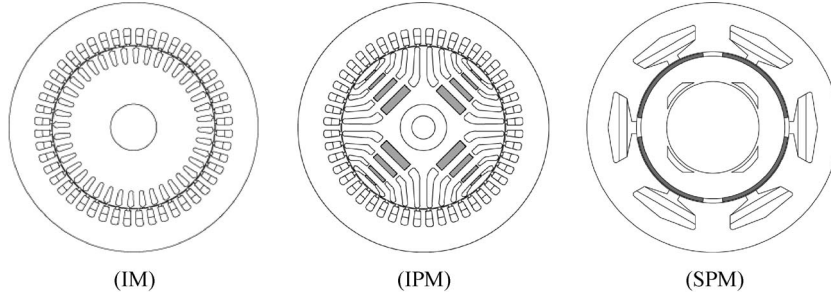
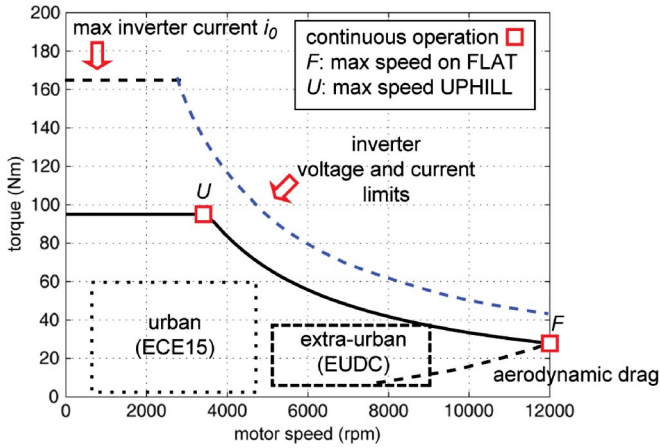Fig. 1. IM, IPM motor, and SPM motor under investigation.

Fig. 2. Example of target specification for an EV.

then, a constant power speed range at higher vehicle speed. The continuous power at maximum speed P_1 determines the maximum speed of the vehicle on flat (**F** red square, for *Flat*). The continuous stall torque T_1 determines the maximum slope that the vehicle can climb continuously (**U** red square, for *Uphill*). Transient overload torque and power are limited by the inverter current rating (i_0), and the combination of voltage and current limits (v_0, i_0), respectively. The typical areas of urban and extra-urban operations are also evidenced in Fig. 2, which will be calculated according to the New European Driving Cycle New European Driving Cycle for the final designs of Section VII. ECE15 and EUDC in Fig. 2 indicate urban and extra urban, according to the NEDC standard [23]. Detailed vehicle specifications are reported in the Appendix.

B. Common Data and Goals of the Comparison

The torque versus speed profiles of Fig. 2 are indicative but not mandatory, except for point F. The three drives under comparison must comply with **the basic requirement of giving the same maximum vehicle speed**, i.e., giving the same continuous power at the maximum motor speed of 12 000 r/min. All the other parameters evidenced in Fig. 2 are matter of the comparison: continuous torque at point U, maximum overload torque at given inverter current, transient overload, and efficiency over the whole operation area and in the preferred maximum efficiency area. The stack outside diameter, stack length, and air-gap length are the same for the three motors,

as well as the same liquid cooling setup. It is assumed that the stator windings are at 130 °C in continuous operation, the PMs are at 150 °C, and the rotor of the IM is at 180 °C. The inverter voltage and current are set to $v_0 = 173$ Vpk phase voltage, corresponding to a 300 V dc link, and $i_0 = 360$ Apk phase current.

III. IM DRIVE

A. Motor Model in the Rotor Field-Oriented Frame

The dq reference frame, synchronous to the rotor flux, is considered. In this frame, the stator flux vector components, at steady state, become

$$\begin{cases} \lambda_{sd} = L_s \cdot i_{sd} \\ \lambda_{sq} = \sigma \cdot L_s \cdot i_{sq} \end{cases} \tag{1}$$

where L_s is the stator self-inductance, σ is the total leakage factor (2), and σL_s is the stator transient inductance

$$\sigma = 1 - \frac{L_M^2}{L_s \cdot L_r}. \tag{2}$$

The steady-state expressions of stator voltage and torque are

$$\bar{v}_{sdq} = R_s \cdot \bar{i}_{sdq} + j\omega \cdot \bar{\lambda}_{sdq} \tag{3}$$

$$T = \frac{3}{2} \cdot p \cdot (\bar{\lambda}_{sdq} \wedge \bar{i}_{sdq}) \tag{4}$$

where ω is the synchronous electrical speed. Last, the slip speed at steady state is

$$\omega_{sl} = \tau_r^{-1} \cdot \left(\frac{i_{sq}}{i_{sd}}\right) \tag{5}$$

where $\tau_r = L_r/R_r$ is the rotor time constant and R_r is the rotor resistance reported to the stator. Independently of the control technique (rotor-field-oriented, stator-field-oriented, direct torque control), the magnetic model (1) can be used in association to (3)–(5) for describing the torque and power curves as a function of rotor speed, at given voltage and current limits [15], [16].

B. Power Curves at Constant Current

The stator current and flux linkage vectors will be indicated, from now on, as flux linkage and current, with no subscript s,
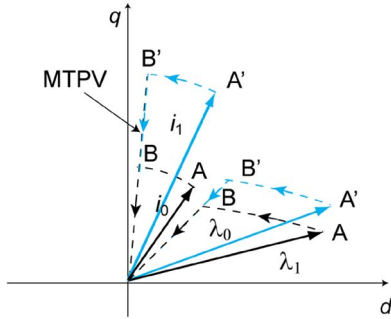
Fig. 3. IM current and flux vector trajectories for maximum power under limited voltage amplitude.

Fig. 5. IPM current and flux vector trajectories for maximum power under limited voltage amplitude.
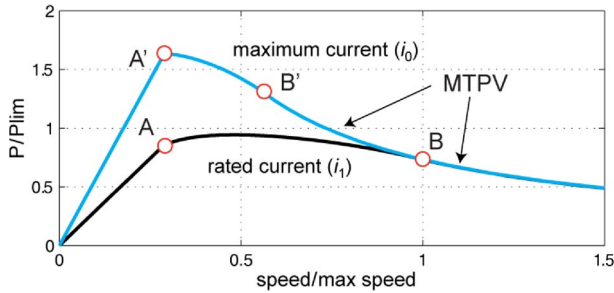

Fig. 4. IM power versus speed curves, for rated and overload current amplitudes and limited voltage.

as also for the other motors described in the following sections. The vector trajectories of the IM drive, corresponding to a given current amplitude, with limited voltage, are qualitatively shown in Fig. 3, along with the corresponding power versus speed curves, shown in Fig. 4. The vector diagrams and power curves are replicated for the continuous current i_1 and for the maximum current i_0. This may not be representative of the actual control trajectories of the drive, but power curves at given voltage and different current limits will be useful here and in the following for comparing the characteristics of the different drives.

It must be underlined that i_0 is the same for all the three drives, which have the same inverter, while i_1 depends on the machine type and will be slightly different for the three motors.

In Fig. 3, the stator current and stator flux linkage vector trajectories are reported [17]. As said, the d-axis is the direction of the rotor-flux linkage vector. At low speed, the maximum torque per ampere (MTPA) condition is considered, which means that the overload point (A') will require a slightly higher d-current component, if compared with the rated current point (A). At higher speeds, the voltage limit requires that the current vector is rotated toward the q-axis (flux-weakening region I), until the flux argument becomes $45°$, i.e., the maximum torque per voltage (MTPV) condition represented as B and B′, respectively. From B (and B′) on, both current and flux vectors are reduced at constant phase angle (flux-weakening region II).

In Fig. 4, the normalized power curves corresponding to rated and overload currents are shown. Unitary speed is the maximum operating speed, while the base power is equal to $P_{lim} = 3/2 \cdot v_0 \cdot i_1$. With this power scale, the A to B region
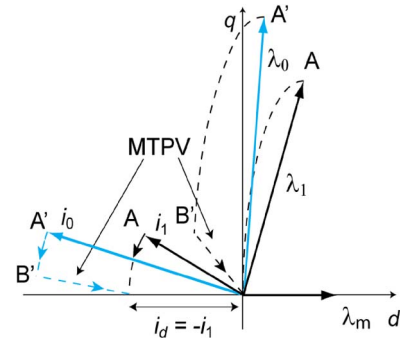
of the power curve at rated current i_1 coincides with the power factor (PF) of the motor, having disregarded the losses. A good design practice is to design a motor having the transient inductance as low as possible, to push the MTPV region at rated current over the maximum speed, or at least not under, as in Fig. 4 (maximum speed is one per unit). This approach maximizes the output power at maximum speed, given the inverter size. At overload, B′ is at a lower speed than B, with how lower depending on the overload ratio i_0/i_1. From point B′ on, the power curve drops to rejoin the rated current curve at point B.

IV. IPM MOTOR DRIVE

A. Motor Model

The voltage vector and torque expressions are formally identical to those of the IM, (3) and (4), respectively. The linear magnetic model of the IPM motor is expressed by

$$\lambda_d = L_d \cdot i_d + \lambda_m$$
$$\lambda_q = L_q \cdot i_q \tag{6}$$

where λ_m is the PM flux linkage and the d, q inductance values are different according to the rotor saliency

$$\xi = \frac{L_q}{L_d} > 1. \tag{7}$$

Due to magnetic saturation, the two inductances (L_q in particular) are variable with the current vector working point, and also, $d - q$ cross-coupling terms should be included in the magnetic (6).

B. Power Curves at Constant Current

The vector trajectories and power curves are reported also for the IPM motor drive, in Figs. 5 and 6, respectively [17], for the case of a motor having high anisotropy and low per-unit PM flux linkage. In this case, the phase angle of the current vector corresponding to MTPA is leading the q-axis by $45°$ or even more [5]: In Fig. 5, point A (rated current) and point A′ (maximum current) represent operation below the base speed. After the voltage limit, the current vector is rotated for flux weakening toward the MTPV locus, if any. Synchronous PM drives actually have a MTPV region (flux-weakening region II)
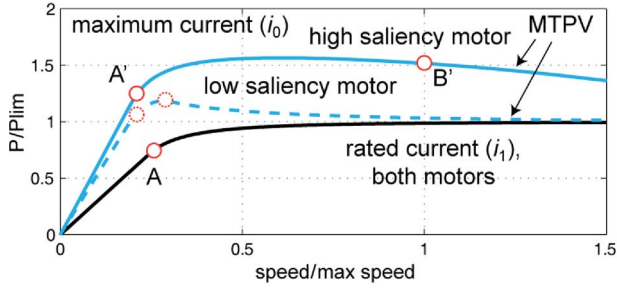
Fig. 6. IPM power versus speed curves (limited voltage), for rated and overload current amplitudes. Effect of rotor saliency on the power overload curve.

Fig. 7. SPM current and flux vector trajectories for maximum power under limited voltage amplitude.

only for current values that are greater than the characteristic current [10]

$$|\bar{i}| > i_{ch} = \frac{\lambda_m}{L_d}. \tag{8}$$

The particular design condition (9) is chosen, where the continuous current equals the motor characteristic current i_{ch} for having an ideally flat power profile at rated current

$$i_1 = i_{ch}. \tag{9}$$

This implies that the MTPV is met only at overload current (e.g., point B′ at maximum current i_0).

In Fig. 6, the power versus speed curves of the IPM motor drive are reported at i_1 and i_0. As for the IM, from base speed on (point A), the per-unit power at i_1 is representative of the PF, due to the scale factor $P_{lim} = 3/2 \cdot v_0 \cdot i_1$, which refers to i_1. The PF at maximum speed is unitary (dark curve, speed equal to 1), while in the same condition, the PF of the IM is lower (0.7 in point B of Fig. 4). Slightly better values are possible for the IM, via the minimization of the transient inductance: The example IM design presented in Section VI will actually have a PF of 0.8 at maximum speed. Still, the better PF of the IPM motor leads to a lower i_1 for the same continuous power, given the inverter voltage.

The power curve at maximum current i_0 is also very flat, due to the high saliency. In Fig. 6, it is also shown, still qualitatively, that a low saliency motor would have a limited power overload capability (dashed overload line), as demonstrated in [5]. Hence, multilayer IPM rotors like the one in Fig. 1 are more suitable for transient power overload, while less salient structures such as single-layer or flux-concentration IPM rotors have the power overload limitations typical of SPM motors, as addressed in the next section.

V. SPM MOTOR DRIVE

A. Motor Model

The linear magnetic model of the SPM motor is expressed by (6) with $L_d = L_q = L$

$$\lambda_d = L \cdot i_d + \lambda_m$$
$$\lambda_q = L \cdot i_q. \tag{10}$$

The single inductance value for both the d, q axes is due to the nonsalient geometry. At a deeper insight, magnetic saturation
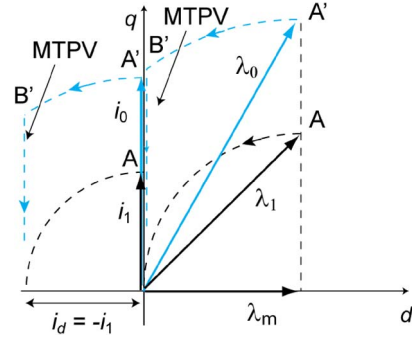
modifies the two inductances, resulting in magnetic saliency ($L_d \neq L_q$) in spite of the geometry, and also produces cross-coupling terms, as for the IPM motor. The voltage and torque expressions are still (3) and (4), respectively, with the latter one becoming very simple when associated to the isotropic model (10)

$$T = \frac{3}{2} \cdot p \cdot \lambda_m \cdot i_q. \tag{11}$$

B. Power Curves at Constant Current

In Fig. 7, the vector trajectories of the SPM motor drive are reported: At low speed, the current vector is along the q-axis (points A and A′), i.e., MTPA operation. At higher speeds, as the voltage limit occurs, the current vector is rotated along the dashed paths for flux weakening. The design condition (9) is chosen also here as for the IPM motor, for the same reason of obtaining a flat power curve at rated current i_1. The MTPV is met when $i_d = -i_{ch} = -i_1$ and the total flux linkage vector is along the q-axis (point B′). Again, MTPV occurs at overload current only, due to the design condition (9). In MTPV operation, the i_d current component remains equal to $-i_{ch}$, and the torque-producing component i_q is progressively reduced, as in Fig. 7.

In Fig. 8, the power versus speed curves of the SPM motor drive are reported, for rated and maximum currents. Both the power curves tend asymptotically to one per unit. According to Fig. 7, the flux linkage in MTPV has no d-axis component, and it is then directly proportional to torque

$$\lambda_{MTPV} \equiv \lambda_q = L \cdot i_q = \frac{L}{\frac{3}{2}p \cdot \lambda_m} \cdot T_{MTPV}. \tag{12}$$

At high speed, the voltage drop across the stator resistance is negligible

$$|\bar{v}_s| \cong \omega \cdot |\bar{\lambda}|. \tag{13}$$

Therefore, from the manipulation of (11)–(13), the torque and power at MTPV are obtained

$$T_{MTPV} = \frac{3}{2}p \cdot \frac{\lambda_m}{L} \cdot \frac{v_0}{\omega} = \frac{3}{2} \cdot \frac{p}{\omega} \cdot i_{ch} \cdot v_0 \tag{14}$$

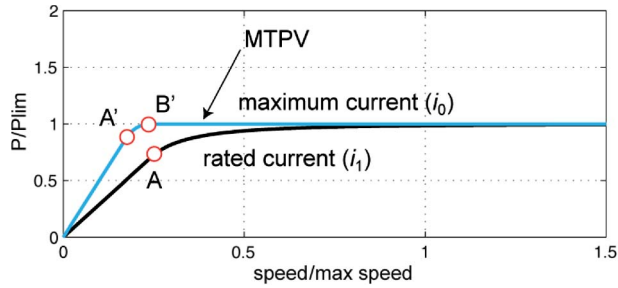$$P_{MTPV} = \frac{3}{2} \cdot i_{ch} \cdot v_0. \tag{15}$$

Fig. 8. SPM power versus speed curves (limited voltage), for rated and overload current amplitudes.

It is then demonstrated that the overload power of SPM motors is upper limited according to the maximum voltage v_0 and the motor characteristic current, **whatever the available overload current is**. With the design choice (9), the MTPV power limit coincides with $P_{lim} = 3/2 \cdot v_0 \cdot i_1$, which is the unitary power in Fig. 8.

VI. DESIGN RESULTS AND POWER CURVES

Three example motors having the same active dimensions are designed and compared by means of FEA. The continuous output power specification is 50 kW at 12 000 r/min. The inverter voltage is 300 V dc, corresponding to 173 Vpk phase voltage (v_0), and the maximum current (i_0) is 360 Apk. The dimensions of the active stack are as follows: 216-mm stator outside diameter and 170-mm active length for the three motors. The motors are water cooled. The ratings of the cooling setup are discussed in the dedicated Section VII-F.

The three motors are designed for having the best compromise between continuous power, transient overload power, and efficiency. All three are comprehensively evaluated by means of 2-D, in terms of magnetic curves, core loss, PM loss, and IM cage loss. The magnetic curves are calculated in all the i_d, i_q operating plane, accounting for saturation effects. End connection additional resistance and inductance terms are evaluated analytically, also for the squirrel cage [11]. In particular, the magnetic curves of the IM are precisely evaluated with the method presented in [12]. The motor laminations are the ones shown in Fig. 1. The significant motor ratings are reported in Table I.

All machines have two pole pairs, for limiting the impact of core and PM losses, given the 12 000-r/min operation. The IM and the IPM motor have the same stator laminations, with 48 slots, i.e., four slots per pole per phase. Such relatively high number of stator slots helps in minimizing the torque ripple and harmonic core loss of the IPM motor [14]. Dealing with the IM, the 48–40 stator–rotor slot combination of Fig. 1(a) is one of the suggested ones in [24].

A counterintuitive result of Table I is that the PM quantity of the IPM motor is higher than the one of the SPM: 1.95 kg versus 1.35 kg. This is related to the 12 000-r/min speed specification, which results in the IPM rotor having very thick structural ribs in Fig. 1(b). The thicker are the ribs, the more of the PM flux is shunted between layer and layer, resulting in an augmented

TABLE I
RATINGS OF THE THREE MOTOR DESIGNS

		IM	IPM	SPM
Pole pairs			2	
Stator slots		48		6
Stator outer diameter	mm		216	
Stator bore diameter	mm	142		131
Stack length	mm		170	
Airgap	mm		0.7	
Number of turns		20		23
Copper fill factor			0.4	
End connections (per side)	mm	150		77
Max speed	rpm		12000	
Continuous torque *	Nm	110	160	130
Speed at continuous torque *	rpm	4000	3800	3800
Current at continuous torque	A pk	200	255	294
Maximum speed **	rpm	11300	12000	10300
Overload torque	Nm	210	210	150
Overload current	A pk	360	360	360
Characteristic current (150°C)	A pk		205	193
Phase rated voltage	V pk	173	173	173
Phase back-emf (12000 rpm, 20°C)	V pk		170	540
Stator resistance (130°C)	Ω	0.027	0.027	0.021
Rotor resistance (180°C)	Ω	0.018		
Steel grade			M250–35A	
PM grade			BMN-42SH	
PM mass	kg		1.95	1.35
Rotor temperature		180° C	150° C	150° C

* Low speed dot, in Fig. 13, at 3200 W dissipation
** High speed dot, in Fig. 13, at 3200 W dissipation

PM quantity. Moreover, the PM quantity could be significantly reduced, as proposed in the recent work [8], and yet not applied to the example machine reported here. Structural ribs have been FEA evaluated against centrifugal stress.

Dealing with the SPMs, those of Fig. 1(c) are particularly thin: They have been verified against demagnetization at 150 °C, but with PM materials of lower grades, they could have problems and should be made thicker. Thicker magnets increase the margin against demagnetization and rebalance the PM material quantities of the two motors.

A. Rated Power Specification

In Fig. 9, the three example designs are compared in terms of output power at given voltage and current. All three have similar torque for the example current, as the power curves at low speed demonstrate. Dealing with high speed, the SPM and IPM motor drives fulfill the continuous power specification of 50 kW at 12 000 r/min with the example current of 216 Apk, which is close to their respective characteristic currents. The IM has a lower output power at high speed and requires a higher current value for the same power. As said, both the PM motors have unitary PF at high speed with the current around i_{ch}, and both their power curves tend to $P_{lim} = 3/2 \cdot v_0 \cdot i_1$, as shown in Figs. 6 and 8, due to the design choice $i_1 = i_{ch}$.
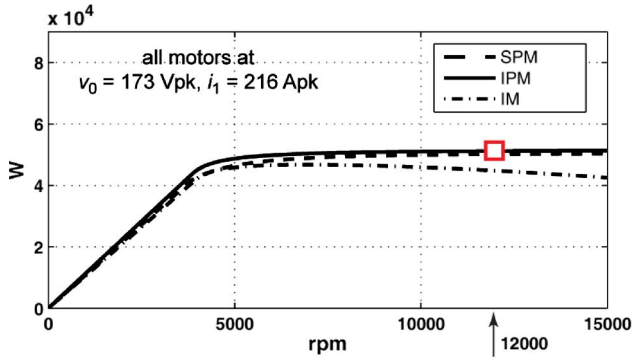
Fig. 9. Power curves of the three motors at same current and voltage. SPM and IPM motors fulfill the continuous power specification with the same current and voltage, while the IM requires a higher current.
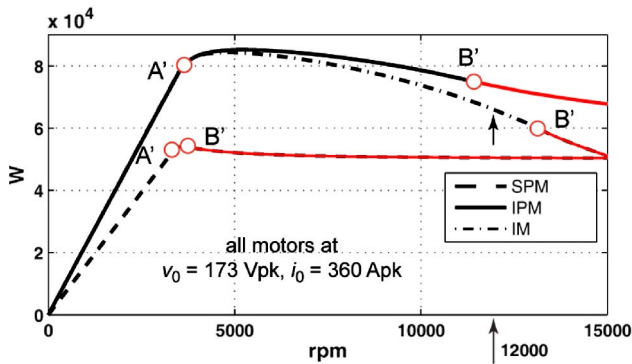

Fig. 10. Power curves of the three motors at maximum current and voltage. The continuous red lines, over point B' of the three curves, indicate the MTPV operating region.

Then, for the same output power, they have nearly the same characteristic current, as in Fig. 9. The IM has a lower output power at the same current and voltage due to the lower PF, as said in Section III-B.

B. Power at Maximum Inverter Current

The power output at maximum current of the three designs is compared in Fig. 10. As said, the SPM motor has no power overload due to the MTPV power clamping. Moreover, also the torque overload is quite limited with respect to the other two motors, due to the hard saturation of the motor core related to the high armature flux at overload, indicated as cross-saturation (the q-current-produced flux reduces the d-flux component, i.e., the torque factor of the machine). The IPM motor and the IM have the same maximum transient overload torque (point A' and speeds below) because, by coincidence, they have exactly the same torque angle at 360 A, MTPA. They both have quite flat power curves. The IPM motor enters the MTPV close to the maximum operating speed and the IM even over the speed rating.

C. Effect of Skewing

All the three motors are skewed for minimizing torque ripple and possible acoustic noise. The IM and IPM motor have
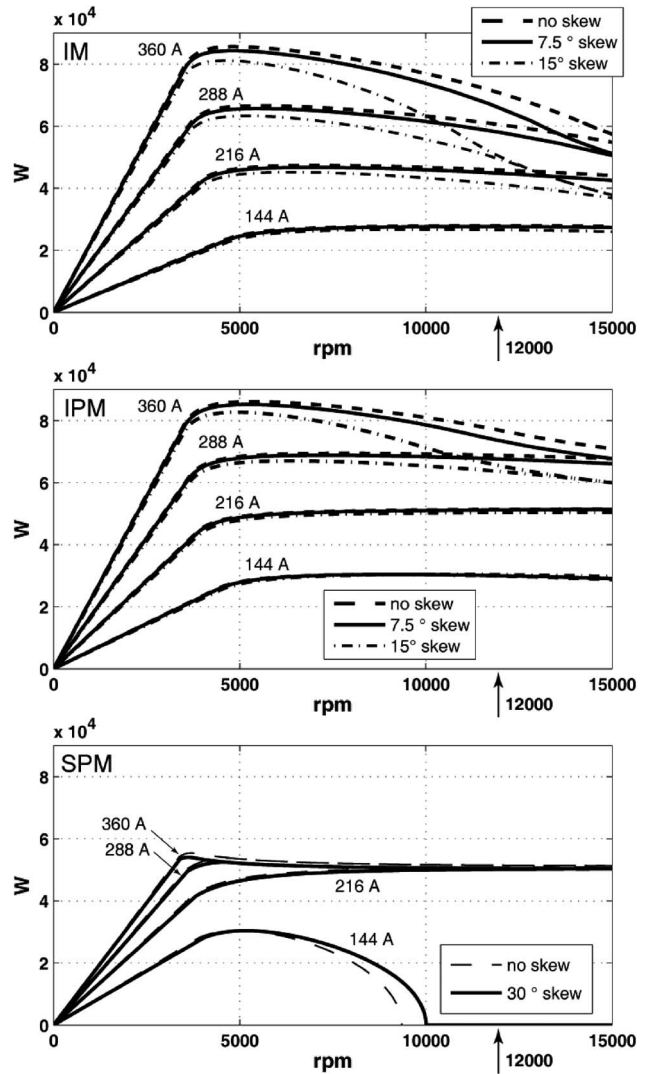

Fig. 11. Effect of skewing on the power curves at constant current and voltage of the three design examples.

the same stator, with 48 slots, and are both skewed by 7.5 mechanical degrees (one stator slot). The SPM motor is skewed by 30 mechanical degrees. The general consequence of skewing is to reduce the average torque and PF, and then output power at high speed. The power curves of the three motors are compared in Fig. 11, for different skew angles.

The continuous power curves of IM and IPM in the top and medium subfigures of Fig. 11 refer to the nominal skewing. In the same graphs, the effect of twice the skewing angle is also shown, stating that motors with lower slot numbers would suffer more power drop due to skewing effects. The SPM power curves (bottom of Fig. 11) are not affected by skewing, despite the large skewing angle due to the low number of slots. This counterintuitive result is justified by the fact that the SPM machine core is quite saturated at no load. The skewed construction results in a machine that is partially less saturated and has nearly the same output characteristics.

In conclusion, skewing has a relatively little impact on the power characteristics of all three motors, even if as a consequence of very different physical reasons.
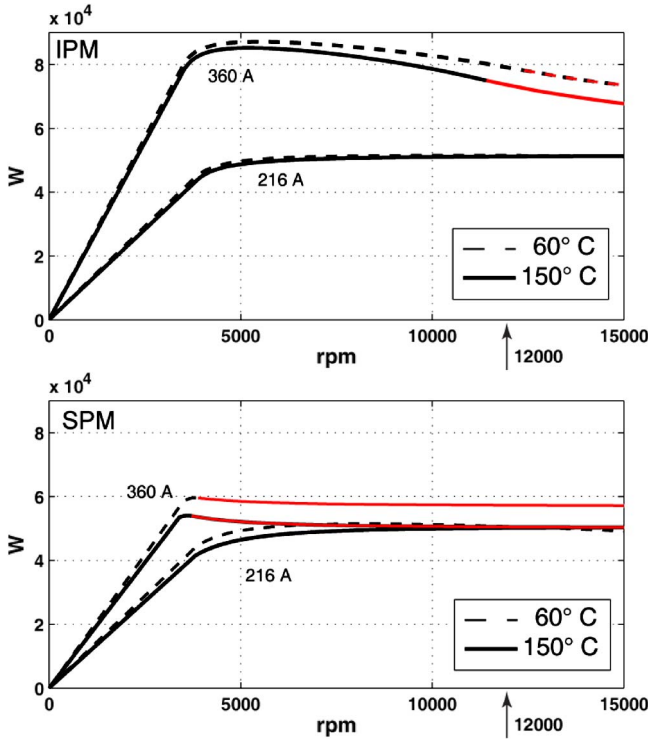
Fig. 12. Effect of PM temperature on the power curves of the IPM and SPM motor designs.

D. Effect of Rotor Temperature

PM temperature is another factor that affects the power curves of PM synchronous motors. In Fig. 12, the operating temperature of 150 °C is compared to the lower value of 60 °C. The SPM overload curve (bottom subfigure) is higher at lower temperature due to the higher i_{ch} in (15), given that the characteristic current varies with temperature as the no-load flux, according to (8). The IPM motor (top subfigure) is less sensitive to temperature variations than the SPM one, as expected from a very salient machine with respect to a non-salient one. In particular, the IPM power curve at rated current is practically insensitive to temperature, while the overload curve reduces more evidently at high speed. The rotor temperature of the IM has a very little effect on the output power curves of the example motor, and they have not been shown in Fig. 12 for space reasons. For example, at 3500 r/min and 100 N · m, the slip speed is 112 r/min at 20 °C and 184 r/min at 180 °C.

VII. LOSS ANALYSIS AND EFFICIENCY

Core losses, PM losses, and rotor cage losses of the IM are FEA evaluated with Infolytica Magnet 7.2, via *transient with motion*, 2-D simulations.

A. FEA Evaluation of Core Losses

Core losses are calculated in postprocessing by means of a modified Steinmetz (16) fitting the manufacturer loss data as a function of flux density and frequency

$$\frac{W}{kg} = k_h \cdot f^\alpha \cdot B^\beta + k_e \cdot f^2 \cdot B^2 \qquad (16)$$

where the values of the coefficients are as follows: $k_h = 0.00778$, $\alpha = 1.23$, $\beta = 1.79$, and $k_e = 3.15e - 005$ for the M250-35A steel grade. The loss model (16) groups the hysteresis and the anomalous loss into a single term, proportional to $(f)^\alpha$. The second term of (16), proportional to $(f)^2$, accounts for eddy-current loss.

For the SPM and IPM motors, a set of simulations at impressed currents is run on a grid covering the respective operating regions in the (i_d, i_q) plane, at rated speed (4000 r/min). This is very similar to what was done for the evaluation of the d, q flux linkages at Section VI, and the set of FEA runs can even be the same both for fluxes and core losses. The output of the simulations is the loss model at reference speed $n_0 = 4000$ r/min. The loss model is in the form of four surfaces (modified hysteresis term and eddy-current term, both for the stator and the rotor), all four as a function of the current components i_d, i_q. For extrapolating the loss at all speeds, the modified hysteresis (h) and the eddy current (e) loss are evaluated in (17) according to the frequency exponents of (16), under the simplifying assumption that the frequency of local flux density variations is proportional to the synchronous speed in all the machine volume

$$\text{Core loss} = (\text{loss})_h \cdot \left(\frac{n}{n_0}\right)^\alpha + (\text{loss})_e \cdot \left(\frac{n}{n_0}\right)^2. \qquad (17)$$

The procedure followed for the IM is similar, although the (d, q) stator current components are not known *a priori* when running a current-impressed FEA of an IM. For simulating the willed (i_d, i_q) condition, a current vector of amplitude $\sqrt{i_d^2 + i_q^2}$, rotating at synchronous speed of 4000 r/min, is imposed into the motor phases. The rotor speed is set to be constant for having a certain slip speed, which reproduces the (i_d, i_q) condition in rotor-flux synchronous coordinates. The relationship between the slip speed and the rotor field oriented control (d, q) current components is known after the static evaluation of the IM magnetic curves introduced at Section VI [12]. The extrapolation of stator loss at different speeds is made by (17), where n is the synchronous speed and not the rotor speed in this case. Rotor core loss is negligible with respect to all other loss terms.

B. FEA Evaluation of PM Losses

PM losses are calculated via the same transient with motion FEA simulations used for core loss calculation, throughout all the (i_d, i_q) operating area. The eddy-current loss in the solid PM material pieces is calculated by Magnet 2-D according to the electrical conductivity of the material, i.e., 1.5e-006 S/m for the BMH-42SH grade. The PM loss of the example IPM motor turns out to be negligible in all conditions. Dealing with the SPM machine, the loss at different speeds is extrapolated according to the square of the mechanical speed. Tangential segmentation is included in the 2-D FEA model, where all magnet poles are made of five segments. Dealing with the effect of axial segmentation, this is evaluated analytically in postprocessing [13]: The example motor is segmented in ten pieces

axialwise. Further segmentation in either directions would not give any practical improvement.

C. FEA Evaluation of IM Cage Losses

IM cage losses are calculated at any operating point by static FEA, with the rotor resistance estimated analytically [12]. This approach does not account for rotor space harmonics. Therefore, spot transient simulations are run for evaluating the additional rotor cage losses of the IM in specific working points, such as target continuous operation points *F* and *U*, showing that the impact of such a loss term is quite limited. Additional losses due to inverter modulation have been FEA calculated, and they are under 200 W in all operation modes, at a 10-kHz switching frequency, with reference to pulsewidth modulation. This loss term will be disregarded in the following.

D. Power Loss Maps

In Fig. 13, the loss maps of the three motors are reported, in the respective torque–speed operating regions. The dashed-line maximum torque profile in each subfigure represents the current and voltage limits of each motor: As already discussed, this is very limited in the SPM case, while the other two motors show little differences and only around maximum speed. The other dashed line is representative of the aerodynamic drag, as defined in Fig. 2. The IM is the one with the highest losses at low speed. At high speed, it is intermediate between IPM and SPM motors. The SPM is the worst solution at high speed because of the PM loss and Joule loss related to the flux-weakening current component (negative i_d). The IPM motor has the lowest losses in all conditions.

E. Continuous Operation and Target Points **F** and **U**

The continuous-line torque profile in all subplots of Fig. 13, the same for all the motors, represents the benchmark of continuous operation. The two reference points *F* and *U*, defined in Fig. 2, are indicated with two square dots. The detail of losses in *F* and *U* is shown in Fig. 14. The total losses are similar for the two PM machines at low speed (point *U*), while at high speed, SPM is heavily penalized by the PM loss. The stator Joule loss of the SPM is the minimum, due to short end connections. IM ones are the maximum, due to the higher current value for the given specification (as said in Section VI-A). The stator core loss of the IPM motor is the highest, due to space harmonic fields.

The loss of the IPM motor at rated power point **F** is 3200 W, both from Figs. 13(b) and 14(a). This loss level is now set as a term of comparison between the three motors at high and low speeds: The blue circles in Fig. 13 and the horizontal line in Fig. 14 all refer to a 3200-W loss. The low-speed blue circle is placed at 3650 r/min, corresponding to 50 km/h. The other one is placed on the intersection between the aerodynamic drag curve and the 3200-W curve. Both the circles stand for the ***feasible continuous operation***, in case the common cooling setup coincides with the one designed for the IPM motor.
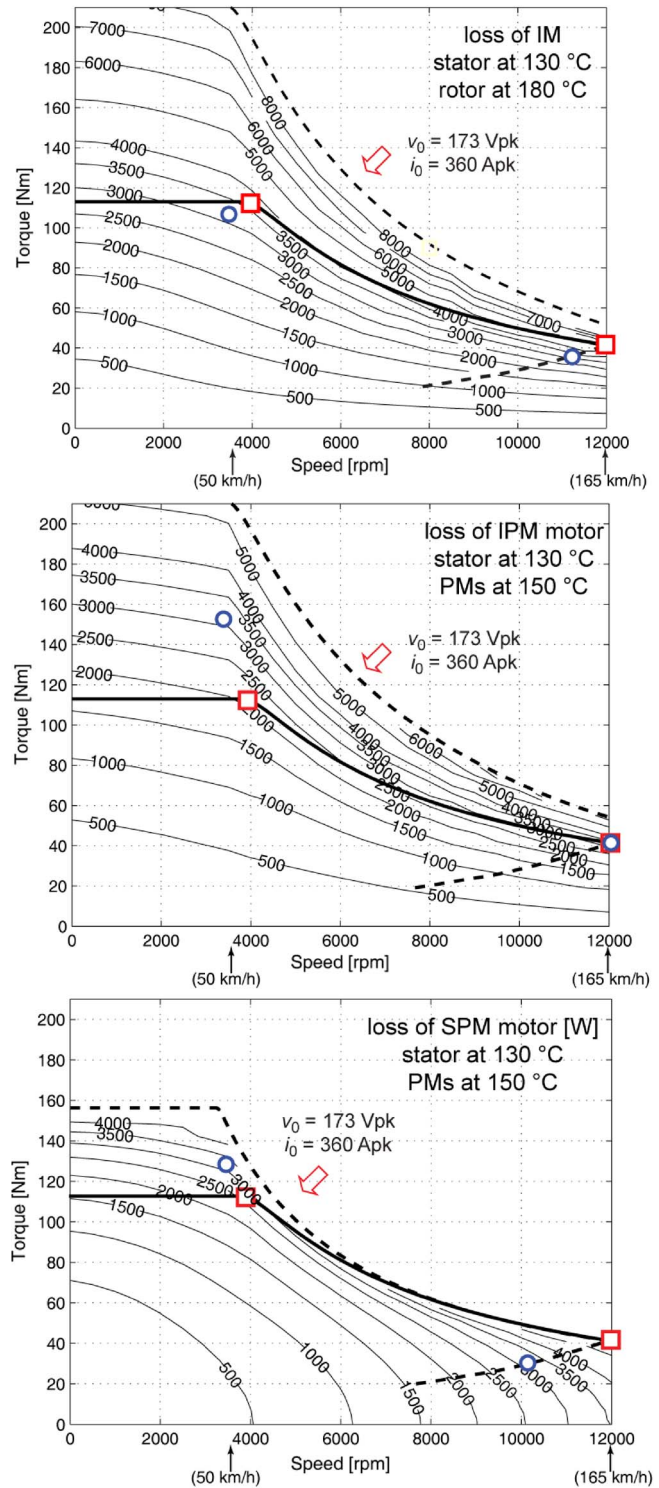

Fig. 13.   Power loss maps of the three designs over the respective torque versus speed operating regions. The torque limit profiles represent (continuous line) the benchmark continuous operation and (dashed line) the inverter limit.

The high-speed circle of the IPM motor [see Fig. 13(b)] coincides with the target point **F**, by definition, and the other one is at 155 N · m, well over the torque of the target point **U**. Dealing with the IM [see Fig. 13(a)], the two circles put in evidence that this is slightly under target both at low and high speeds, due to rotor losses. The SPM motor [see Fig. 13(c)] behaves well at low speed and has problems at high speed: At
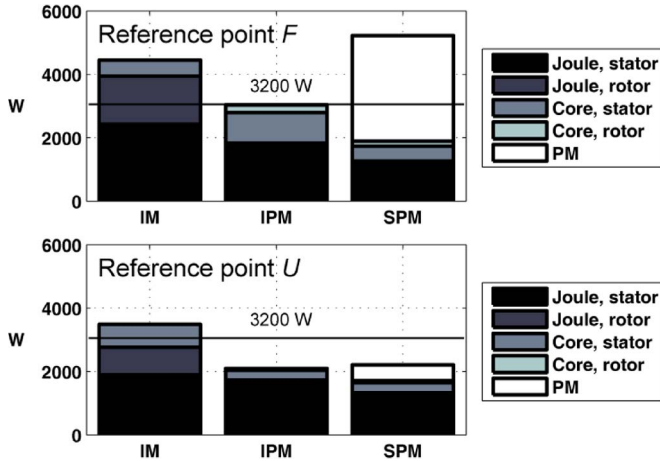
Fig. 14. Loss detail in the reference points defined in Fig. 2: (a) Point F is 39 N · m, 12 000 r/min. (b) Point U is 110 N · m, 4000 r/min.

50 km/h, the continuous torque is over U, still with a torque that is lower than the one of the IPM motor, for the reasons described at Section V and in [5]. High-speed operation would be limited, under the 3200-W loss assumption, to 10 300 r/min, due to the very high PM loss [see Fig. 14(a)], despite the axial and the tangential segmentation of the magnets. The feasible continuous operation is the one referred to in Table I, indicated with starred values.

F. Feasibility of the Cooling Setup

The IPM loss of 3200 W corresponds to a specific heat removal of 26 kW/m^2, with reference to the outer surface of the stator stack: 216-mm diameter and 170-mm length, i.e., 0.115 m^2. This is supposed to be a special cooling setup, out of the industrial standard for electric motors.

An example of an experimental cooling setup is the one reported in [19], for a prototype motor for hybrid electric traction, with a target speed of 14 000 r/min. The liquid cooling has the same flow rate considered here (10 L/min) and a higher inlet temperature (105 °C), related to the combustion engine coolant temperature. The prototype in [19] is stopped at 7500 r/min for temperature limits, with a specific heat flow of 19 kW/m^2. The target speed of 14 000 r/min would require something like 56 kW/m^2.

Owing to the lower inlet liquid temperature (60 °C), possible in a purely EV, the cooling target of 26 kW/m^2 may be considered realistic. Of course, the trend of having very dense motors in traction, with high speed ratings, requires the cooling setups to be designed purposely.

G. New European Driving Cycle

The three motors are compared in terms of energy consumption, with reference to the NEDC, which consists of four repeated ECE-15 European Urban Driving Cycle driving cycles and an Extra-Urban Driving Cycle (EUDC) [23]. The vehicle data are reported in the Appendix.

The results, in watts per hour, are shown in Fig. 15 and refer to regenerative braking conditions. Motor loss only is
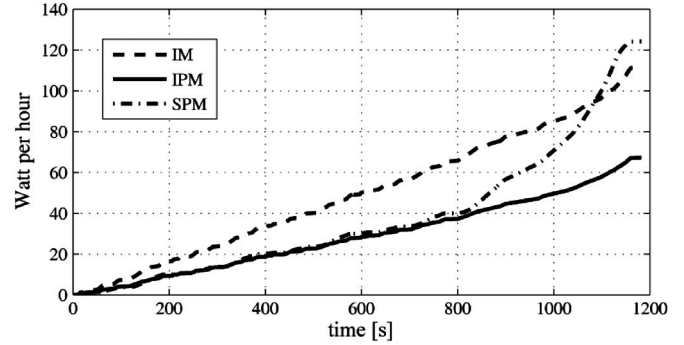

Fig. 15. Energy loss over the NEDC for the three motors.

considered here: The other loss components of the power train, which are those of the battery and the power converters, are out of this comparison. IPM and SPM motors are very similar in the first part of the cycle, referring to urban operation. In suburban operation (from time 800 s on), the higher vehicle speed penalizes the SPM. The IM has definitely higher loss than the IPM one, but both motors have a constant rate of energy consumption all over the cycle time: More frequent starts and stops in urban areas (0 to 800 s) produce the same power loss than less frequent speed variations at higher vehicle speed (800 to 1200 s).

H. Efficiency Maps

In Fig. 16, the efficiency maps are reported, giving better evidence of the NEDC results and of the loss impact in the different areas: The areas corresponding to the urban and sub-urban (ECE15) and extra-urban (EUDC) sections of the New European Driving Cycle are evidenced by dashed squares. The efficiencies in the ECE15 area of IPM and SPM are comparable, as also shown in Fig. 15, between 0 and 800 s, and they are both higher than the efficiency of the IM. The EUDC covers the respective high efficiency areas of the IM and the IPM motor, with the latter being better than the former, while the efficiency of the SPM motor drops significantly in this area due to speed-related losses.

VIII. DISCUSSION

The comparison of the three motor designs leads to the following considerations.

1) Both the SPM and IPM motors give the rated 50 kW at 12 000 r/min for the same current level (216 A), which is close to the respective characteristic currents. The power curves of the two motors are practically identical at this current level (see Fig. 9).
2) The SPM motor has no power overload at higher current levels (see Fig. 10).
3) Also, overload torque is very limited because, at current overload, the armature flux heavily saturates the machine core (Fig. 10, low-speed region).
4) The PM loss at high speed is very high, despite magnet segmentation and the low number of pole pairs.
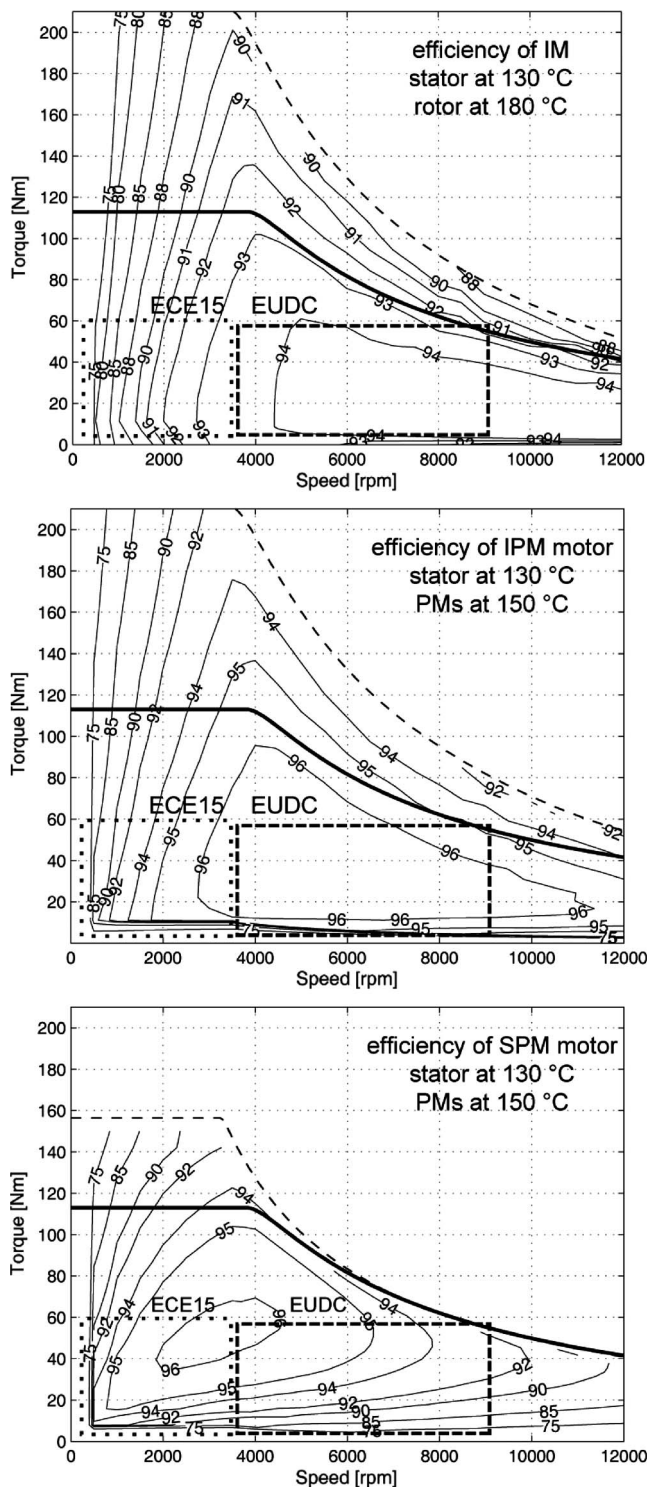5) As a consequence, the maximum vehicle speed in continuous operation should be derated by a factor of 10 200

Fig. 16.   Efficiency maps of the three designs.

layers might behave like the low saliency motor of Fig. 6, while machines with lower numbers of stator and rotor slots might incur less indulgent harmonic loss at high speed [14].

7) The IM needs more current for giving the rated 50 kW at 12 000 r/min (see Fig. 9) due to the lower PF.

8) The lower PF also implies a higher stator current for fulfilling the continuous operation point *F*: In Fig. 14, top diagram, the stator Joule loss of the IM is higher than the one of the IPM with the same stator, due to the PF.

9) Moreover, the IM motor is penalized, with respect to the IPM motor, by the cage losses (see Fig. 14).

10) Nevertheless, the IM has a very good overload capability: At low speed, the torque at maximum inverter current is the same as the one of the IPM motor (Fig. 10, point A′).

IX. CONCLUSION

The performances of three ac motor drives for electric traction are compared. The three design examples have the same stack and inverter size and the same cooling. The three designs are FEA evaluated, and all main aspects of magnetic and loss modeling are accounted for.

The SPM motor has severe limitations at overload, independently of the available inverter current, and at high speed, due to PM loss.

The IPM motor has the better overall performance, in terms of power overload curve and efficiency at any load and any speed, provided that it is a high saliency machine, maximized by proper design.

The IM has overload power curves that are not far from the ones of the IPM, provided that it is designed to have the lowest possible transient reactance. In terms of loss and energy consumption, this is penalized by the cage losses both at low and high speeds.

All considered, the example motors show that it is not always true that SPM machines are more compact and more torque dense than any other machine.

APPENDIX

The vehicle data used for evaluating the NEDC in Section VII are reported in Table II.

to 12 000 r/min if the same heat dissipation is considered for the SPM and the IPM competitor (Fig. 13, bottom, blue circle).

6) Dealing with the IPM motor, the good performance is a consequence of the 48-slot-stator four-layer-rotor design—this produces a high saliency, resulting in the good overload capability and an optimal torque versus harmonic loss compromise. Machines with less rotor

TABLE II
VEHICLE SPECIFICATION

Vehicle mass	kg	1064
Wheels inertia	kg·m²	2.8
Motor + transmission inertia	kg·m²	0.02
Wheel radius	m	0.285
Frontal area	m²	1.8
Drag coefficient		0.39
Rolling coefficient	(km/h)⁻¹	3.3·10⁻⁵
Static friction coefficient		0.0116
Motor to wheel speed ratio		7.8
Transmission efficiency		0.94
Max vehicle speed	km/h	165

REFERENCES

[1] Z. Q. Zhu and D. Howe, "Electrical machines and drives for electric, hybrid, and fuel cell vehicles," *Proc. IEEE*, vol. 95, no. 4, pp. 746–765, Apr. 2007.

[2] K. T. Chau, C. C. Chan, and C. Liu, "Overview of permanent-magnet brushless drives for electric and hybrid electric vehicles," *IEEE Trans. Ind. Electron.*, vol. 55, no. 6, pp. 2246–2257, Jun. 2008.

[3] A. M. El-Refaie and T. M. Jahns, "Comparison of synchronous PM machine types for wide constant-power speed range operation," in *Conf. Rec. 40th IEEE IAS Annu. Meeting*, Oct. 2–6, 2005, vol. 2, pp. 1015–1022.

[4] A. M. EL-Refaie and T. M. Jahns, "Optimal flux weakening in surface PM machines using fractional-slot concentrated windings," *IEEE Trans. Ind. Appl.*, vol. 41, no. 3, pp. 790–800, May/Jun. 2005.

[5] G. Pellegrino, A. Vagati, P. Guglielmi, and B. Boazzo, "Performance comparison between surface-mounted and interior PM motor drives for electric vehicle application," *IEEE Trans. Ind. Electron.*, vol. 59, no. 2, pp. 803–811, Feb. 2012.

[6] T. M. Jahns and V. Caliskan, "Uncontrolled generator operation of interior PM synchronous machines following high-speed inverter shutdown," *IEEE Trans. Ind. Appl.*, vol. 35, no. 6, pp. 1347–1357, Nov./Dec. 1999.

[7] P. Xue and J. Lin, "Discussion on the rare earth resources and its development potential of Inner Mongolia of China," in *Proc. ICMREE*, May 20–22, 2011, vol. 1, pp. 9–12.

[8] P. Guglielmi, B. Boazzo, E. Armando, G. Pellegrino, and A. Vagati, "Magnet minimization in IPM-PMASR motor design for wide speed range application," in *Proc. IEEE ECCE*, Sep. 17–22, 2011, pp. 4201–4207.

[9] S. Ooi, S. Morimoto, M. Sanada, and Y. Inoue, "Performance evaluation of a high power density PMASynRM with ferrite magnets," in *Proc. IEEE ECCE*, Sep. 17–22, 2011, pp. 4195–4200.

[10] W. L. Soong and T. J. E. Miller, "Field-weakening performance of brushless synchronous ac motor drives," *Proc. Inst. Elect. Eng.—Elect. Power Appl.*, vol. 141, no. 6, pp. 331–340, Nov. 1994.

[11] A. Boglietti, A. Cavagnino, and M. Lazzari, "Computational algorithms for induction-motor equivalent circuit parameter determination—Part I: Resistances and leakage reactances," *IEEE Trans. Ind. Electron.*, vol. 58, no. 9, pp. 3723–3733, Sep. 2011.

[12] L. Alberti, N. Bianchi, and S. Bolognani, "Variable-speed induction machine performance computed using finite-element," *IEEE Trans. Ind. Appl.*, vol. 47, no. 2, pp. 789–797, Mar./Apr. 2011.

[13] P. Sergeant and A. Van den Bossche, "Segmentation of magnets to reduce losses in permanent-magnet synchronous machines," *IEEE Trans. Magn.*, vol. 44, no. 11, pp. 4409–4412, Nov. 2008.

[14] G. Pellegrino, P. Guglielmi, A. Vagati, and F. Villata, "Core losses and torque ripple in IPM machines: Dedicated modeling and design tradeoff," *IEEE Trans. Ind. Appl.*, vol. 46, no. 6, pp. 2381–2391, Nov./Dec. 2010.

[15] X. Xu and D. W. Novotny, "Selection of the flux reference for induction machine drives in the field weakening region," *IEEE Trans. Ind. Appl.*, vol. 28, no. 6, pp. 1353–1358, Nov./Dec. 1992.

[16] S.-H. Kim and S.-K. Sul, "Maximum torque control of an induction machine in the field weakening region," *IEEE Trans. Ind. Appl.*, vol. 31, no. 4, pp. 787–794, Jul./Aug. 1995.

[17] N. Bianchi and S. Bolognani, "Unified approach to the analysis and design of an ac motor drive for flux-weakening operations," in *Conf. Rec. 33rd IEEE IAS Annu. Meeting*, Oct. 12–15, 1998, vol. 1, pp. 95–102.

[18] K. Yamazaki, M. Shina, Y. Kanou, M. Miwa, and J. Hagiwara, "Effect of eddy current loss reduction by segmentation of magnets in synchronous motors: Difference between interior and surface types," *IEEE Trans. Magn.*, vol. 45, no. 10, pp. 4756–4759, Oct. 2009.

[19] A. M. EL-Refaie, J. P. Alexander, S. Galioto, M. R. Shah, K.-K. Huh, W. D. Gerstler, J. Tangudu, and T. M. Jahns, "Scalable, low-cost, high performance IPM motor for hybrid vehicles," in *Proc. 19th ICEM*, Sep. 6–8, 2010, pp. 1–6.

[20] A. El-Refaie, T. M. Jahns, P. J. McCleer, and J. W. McKeever, "Experimental verification of optimal flux weakening in surface PM machines using concentrated windings," in *Conf. Rec. 40th IEEE IAS Annu. Meeting*, Oct. 2–6, 2005, vol. 2, pp. 1050–1057.

[21] G.-H. Kang, J.-P. Hong, G.-T. Kim, and J.-W. Park, "Improved parameter modeling of interior permanent magnet synchronous motor based on finite element analysis," *IEEE Trans. Magn.*, vol. 36, no. 4, pp. 1867–1870, Jul. 2000.

[22] K. Yamazaki and N. Fukushima, "Experimental validation of iron loss model for rotating machines based on direct eddy current analysis of electrical steel sheets," in *Proc. IEEE IEMDC*, May 3–6, 2009, pp. 851–857.

[23] DieselNet, Emission Test Cycles—Summary of Worldwide Engine and Vehicle Test Cycles. [Online]. Available: http://www.dieselnet.com/standards/cycles/ece_eudc.php

[24] P. Alger, *Induction Machines, Their Behavior and Uses*, 2nd ed. New York: Gordon and Breach, 1970.

Gianmario Pellegrino (M'06) received the M.Sc. and Ph.D. degrees in electrical engineering from the Politecnico di Torino, Turin, Italy, in 1998 and 2002, respectively.

He was a Guest Researcher at Aalborg University, Aalborg, Denmark, in 2002. Since 2002, he has been with the Politecnico di Torino, first as a Research Associate and then as an Assistant Professor since 2007. He was a Visiting Fellow at Nottingham University, Nottingham, U.K., in 2010/2011. He is involved in research projects within the industry. He has more than 50 technical papers and is the holder of one patent. His research areas include electrical machines and drives, namely, motor design and digital control.

Dr. Pellegrino is an Associate Editor for the IEEE TRANSACTIONS ON INDUSTRY APPLICATIONS. He is the corecipient of the IEEE Industry Applications Society (IAS) Electric Machines Committee 3rd Prize Paper Award for the Energy Conversion Congress and Exhibition (ECCE) 2009, the IEEE-IAS Industrial Drives Committee 3rd Prize Paper Award for ECCE 2010, and the International Conference on Electrical Machines 2010 Best Paper Award.

Alfredo Vagati (M'88–SM'92–F'98) received the Laurea degree in electrical engineering from the Politecnico di Torino, Turin, Italy, in 1970.

After a few years working in industry with Olivetti, he joined the Politecnico di Torino in 1975 as an Assistant Professor. In 1990, he became a Professor of Electrical Machines and Drives at the University of Cagliari, Cagliari, Italy. In 1991, he rejoined the Politecnico di Torino in the same capacity. From 1995 to 2003, he was the Head of the Department of Electrical Engineering, Politecnico di Torino, and he was a member of the Academic Senate from 2005 to 2009. His scientific activity, in the field of electrical machines and drives, has been focused on high-performance ac drives. He has been involved in several industrial projects in the field of ac drives, as both a designer and a scientific reference. His most relevant activity has concerned the design and control of a family of newly developed high-performance synchronous reluctance and permanent-magnet-assisted synchronous reluctance motors. He has led several national and European research projects in the field of the design and control of synchronous-machine-based drives for many different applications, including home appliances and the automotive world. He has authored or coauthored more than 100 technical papers.

Prof. Vagati is a member of the Advisory Board of the Power Conversion and Intelligent Motion International Conference and Exhibition.

Barbara Boazzo received the M.Sc. degree in electrical engineering from the Politecnico di Torino, Turin, Italy, in 2010, where she is currently working toward the Ph.D. degree, working in the field of electric motors and drives.

Paolo Guglielmi (M'07) received the M.Sc. degree in electronic engineering and the Ph.D. degree in electrical engineering from the Politecnico di Torino, Turin, Italy, in 1996 and 2001, respectively.

In 1997, he joined the Department of Electrical Engineering, Politecnico di Torino, where he became an Assistant Professor in 2002 and an Associate Professor in 2012. He has authored several papers published in technical journals and conference proceedings. His fields of interest include power electronics, high-performance drives, and computer-aided design of electrical machines.